

Crossover from itinerant-electron to localized-electron behavior in  $\text{Sr}_{1-x}\text{Ca}_x\text{CrO}_3$  perovskite solid solution

This article has been downloaded from IOPscience. Please scroll down to see the full text article.

2011 J. Phys.: Condens. Matter 23 355601

(<http://iopscience.iop.org/0953-8984/23/35/355601>)

View [the table of contents for this issue](#), or go to the [journal homepage](#) for more

Download details:

IP Address: 159.226.37.158

The article was downloaded on 19/08/2011 at 10:29

Please note that [terms and conditions apply](#).

# Crossover from itinerant-electron to localized-electron behavior in $\text{Sr}_{1-x}\text{Ca}_x\text{CrO}_3$ perovskite solid solution

Youwen Long<sup>1</sup>, Liuxiang Yang<sup>1</sup>, Yuxi Lv<sup>1</sup>, Qingqing Liu<sup>1</sup>,  
Changqing Jin<sup>1</sup>, Jianshi Zhou<sup>2</sup> and John B Goodenough<sup>2</sup>

<sup>1</sup> Institute of Physics, Chinese Academy of Sciences, Beijing 100190, People's Republic of China

<sup>2</sup> Texas Materials Institute, University of Texas, 1 University Station, C2200, Austin, TX 78712, USA

E-mail: [ywlong@iphy.ac.cn](mailto:ywlong@iphy.ac.cn) and [Jin@iphy.ac.cn](mailto:Jin@iphy.ac.cn)

Received 17 May 2011, in final form 26 July 2011

Published 18 August 2011

Online at [stacks.iop.org/JPhysCM/23/355601](http://stacks.iop.org/JPhysCM/23/355601)

## Abstract

Polycrystalline samples of the perovskite family  $\text{Sr}_{1-x}\text{Ca}_x\text{CrO}_3$  have been prepared at high pressure and temperature in steps of 1/6 over the range  $0 \leq x \leq 1$ . Rietveld analysis shows a series of structural phase transitions from cubic to tetragonal to orthorhombic with increasing  $x$ . The cubic samples have no long-range magnetic order; the other samples become antiferromagnetically ordered below a  $T_N$  that increases with  $x$ . At ambient pressure, the electric transport properties of the cubic and tetragonal phases are semiconducting with a small (meV range) activation energy that increases with  $x$ ; the orthorhombic phase exhibits variable-range hopping rather than the small-polaron behavior typically found for mixed-valent, localized-electron configurations. Above a pressure  $P = P_C$ , a smooth insulator–metal transition is found at a  $T_{IM}$  that decreases with increasing  $P$  for a fixed  $x$ ;  $P_C$  increases with  $x$ . These phenomena are rationalized qualitatively with a  $\pi^*$ -band model having a width  $W_\pi$  that approaches crossover from itinerant-electron to localized-electron behavior as  $W_\pi$  decreases with increasing  $x$ . The smaller size of the  $\text{Ca}^{2+}$  ion induces the structural changes and the greater acidity of the  $\text{Ca}^{2+}$  ion is primarily responsible for narrowing  $W_\pi$  as  $x$  increases.

(Some figures in this article are in colour only in the electronic version)

## 1. Introduction

Since 1967 [1], it has been recognized that the  $\text{Cr}^{4+}:3d^2$  electron configuration changes from itinerant-electron behavior in  $\text{SrCrO}_3$  to strongly correlated electron behavior in  $\text{CaCrO}_3$ , but a systematic study of the evolution of the transition from itinerant to strongly correlated electronic behavior in  $\text{Sr}_{1-x}\text{Ca}_x\text{CrO}_3$  solid solution was little known because these perovskites can only be synthesized under high pressure. Recently,  $\text{SrCrO}_3$  and  $\text{CaCrO}_3$  have received renewed interest due to the findings of an anomalous electronic state, microstrain-sensitive phase separation and orbital ordering [2–5]. Castillo-Martínez *et al* prepared  $\text{Sr}_{1-x}\text{Ca}_x\text{CrO}_3$  solid solution and studied the structural properties in detail [6, 7]. Unfortunately, however, considerable

impurity phases, which varied from 10% to 25% in weight for  $x \geq 0.2$ , existed in their samples. It is therefore desirable to prepare higher quality samples and study the intrinsic physical properties.

It is also of interest to compare the properties of the  $\text{Sr}_{1-x}\text{Ca}_x\text{CrO}_3$  system with those of the  $\text{RVO}_3$  ( $\text{R} = \text{rare-earth}$ ) perovskites in which the  $\text{V}^{3+}:3d^2$  configuration is localized for all  $\text{R}^{3+}$  ions. The  $\text{Cr}^{4+}$  and  $\text{V}^{3+}$  ions in these  $\text{AMO}_3$  perovskites occupy corner-shared octahedral sites in which the strength of the  $(180^\circ - \phi)$   $\text{M-O-M}$  interactions ( $\text{M} = \text{transition metal}$ ) determines whether the electrons are localized or itinerant. Moreover, the octahedral-site cubic-field splitting of a  $3d^2$  configuration into a  $t^2e^0$  configuration does not fully quench the orbital angular momentum of the threefold-degenerate  $\pi$ -bonding  $t$  orbitals

$xy$ ,  $yz \pm izx$ . However, in the  $RVO_3$  system, a cooperative rotation of the  $VO_{6/2}$  octahedra lowers the crystal symmetry from its ideal cubic-perovskite structure with  $180^\circ$  M–O–M bonds to orthorhombic; and in the orthorhombic structure, local octahedral-site distortions split the threefold-degenerate  $t$  orbitals, suppressing the orbital angular momentum [8]. These distortions bias the ordering of the  $t$  orbitals in the  $RVO_3$  perovskites [9].  $CaCrO_3$  has the same orthorhombic structure whereas  $SrCrO_3$  has the ideal cubic structure [10, 11].

In this paper, we report on the synthesis of higher quality  $Sr_{1-x}Ca_xCrO_3$  perovskite solid solution. By using a  $\pi^*$ -band model, the electronic state evolution from itinerant-electron to localized-electron behavior is studied on the basis of systematic changes in the crystal structure, electric transport, magnetism, and pressure-induced insulator–metal transitions.

## 2. Experimental details

Polycrystalline  $Sr_{1-x}Ca_xCrO_3$  samples were prepared by using a high pressure and high temperature technique with highly pure SrO, CaO, and  $CrO_2$  starting materials. The pressure we used was 6.0 GPa, and the temperature was changed from 900 to 1200 °C with a step of 25 °C to find the optimum synthesis condition for each sample. The appropriate reactants were thoroughly mixed and then pressed into pellets 6 mm in diameter and about 2 mm in height. After packaging in Pt foil, the pellets were inserted into pyrophyllite assemblies. Graphite tubes were used as heaters. Pressure was generated by a cubic-anvil-type high pressure apparatus. In order to obtain single-phase  $SrCrO_3$  and  $CaCrO_3$ , a 5% and 10%, respectively, excess SrO and CaO was used; the excess CaO and SrO after the reaction was washed out with dilute acid [10]. All the samples were black.

The sample quality and crystal structure were determined using powder x-ray diffraction (XRD) with a Rigaku diffractometer equipped with monochromatic Cu  $K\alpha$  radiation (50 kV, 200 mA). Diffraction data were collected in the  $2\theta$  range from 20 to  $135^\circ$  in steps of  $0.02^\circ$ . The counting time at each step was 5 s. Crystallographic parameters were obtained by a Rietveld full-profile refinement made with the GSAS program [12].

Four-probe ambient-pressure resistivity measurements were made in zero and 6 T magnetic fields from 5 to 300 K. The temperature and magnetic field dependence of the magnetization were measured with a commercial superconducting quantum interference device (Quantum Design, MPMS-5). A four-probe method was used to measure the resistance under pressure in a diamond-anvil cell; the culet of the diamond was 800  $\mu\text{m}$  in diameter. T301 stainless steel was used as a gasket in which a 300  $\mu\text{m}$  hole was drilled as the sample chamber. A bulk sample of about  $100 \times 50 \times 50 \mu\text{m}^3$  was carefully loaded into the gasket chamber. Gold wires with 12  $\mu\text{m}$  diameter were used as electrical probes. To obtain a satisfactory hydrostatic environment, fine MgO powder (1  $\mu\text{m}$  in diameter) was used for the pressure-transmitting medium. In addition, the gasket was covered with a thin layer of

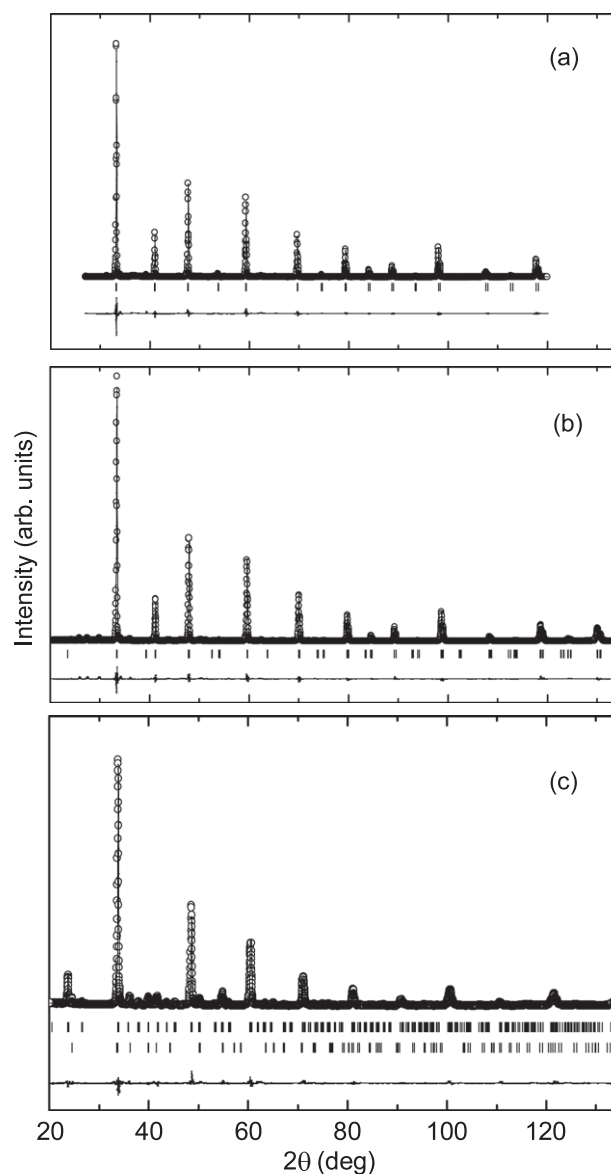


**Figure 1.** Powder XRD patterns and Rietveld refinements for (a)  $x = 0$ , (b)  $x = 1/3$ , and (c)  $x = 1$  samples in the  $Sr_{1-x}Ca_xCrO_3$  family. Observed ( $\circ$ ), calculated (solid line) and difference (below) profiles are shown. The ticks show allowed Bragg reflections. The bottom ticks in (c) present the reflections of a small amount of  $Cr_2O_3$  impurity phase (6.7 wt%).

$Al_2O_3$  powder to prevent any short circuit of the electrical probes. Pressures were calibrated by the ruby-fluorescence method [13].

## 3. Results

### 3.1. Crystal structures

Figures 1(a)–(c) display the results of the Rietveld analysis of three representative samples of the  $Sr_{1-x}Ca_xCrO_3$  system. For  $x = 0$  and  $1/6$ , the XRD data fit well with the ideal simple-cubic structure, space group  $Pm\bar{3}m$  (No. 221) as shown for  $x = 0$  in figure 1(a). For  $x = 1/3$  and  $1/2$ , the room-temperature symmetry changes to tetragonal, space

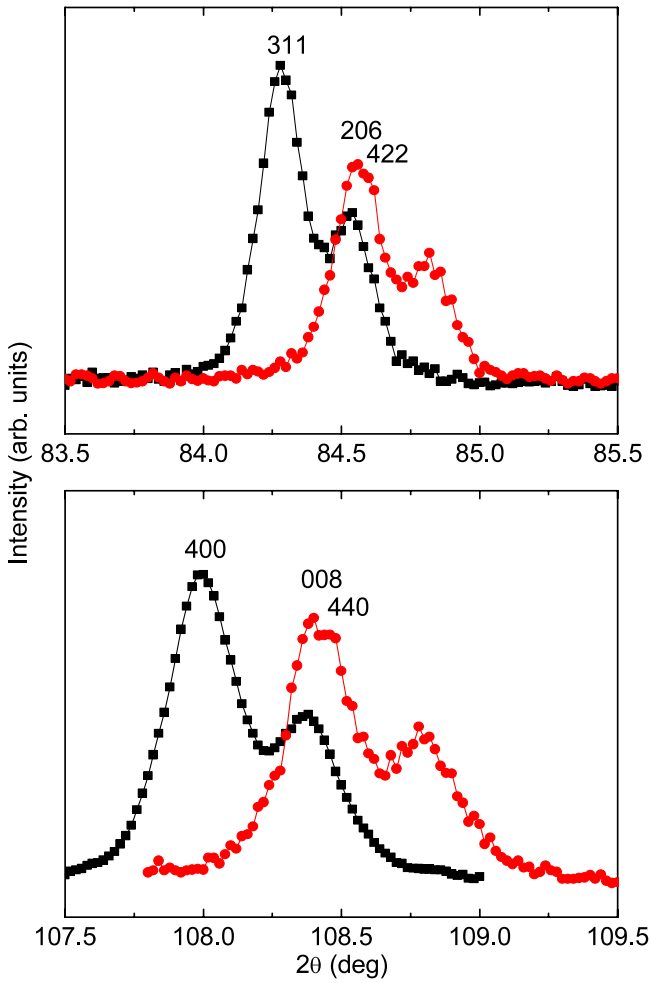


**Figure 2.** Diffraction peak splitting during the structural phase transition from cubic  $Pm3m$  with  $x = 1/6$  (squares) to tetragonal  $I4/mcm$  with  $x = 1/3$  (circles) in the  $Sr_{1-x}Ca_xCrO_3$  family.

group  $I4/mcm$  (No. 140), as shown for  $x = 1/3$  in figure 1(b). In the tetragonal structure, a cooperative opposite rotation of the  $CrO_{6/2}$  octahedra about the  $c$  axis splits the cubic 311 peak into 206 and 422, and the cubic 400 peak into 008 and 440 as shown in figure 2. This cooperative rotation does not require a distortion of the local octahedra, but it bends from  $180^\circ$  the Cr–O–Cr bonds in the  $a$ – $b$  plane. The  $x = 5/6$  and 1.0 samples are refined in the orthorhombic space group  $Pbnm$  (No. 62) as shown in figure 1(c), where the cooperative  $CrO_{6/2}$ -site rotations give the  $a^+b^-b^-$  tilting system in the Glazer notation [14]. The sample with  $x = 2/3$  appears to be a two-phase one; it refines in both the tetragonal  $I4/mcm$  and orthorhombic  $Pbnm$  symmetries. It should be noted that a small amount of  $Cr_2O_3$  impurity phase which increases with increasing  $x$  is identified in our samples. In the end member of  $CaCrO_3$  with  $x = 1$ , the impurity phase is determined to be 6.7 wt% (see figure 1(c)). This value is much less than the impurity amount reported in [6] (about 16 wt%). Fortunately, the influence of the impurities on the intrinsic properties of the perovskite phases does not appear to be significant, but they do signal the presence of cation vacancies in the perovskite phases.

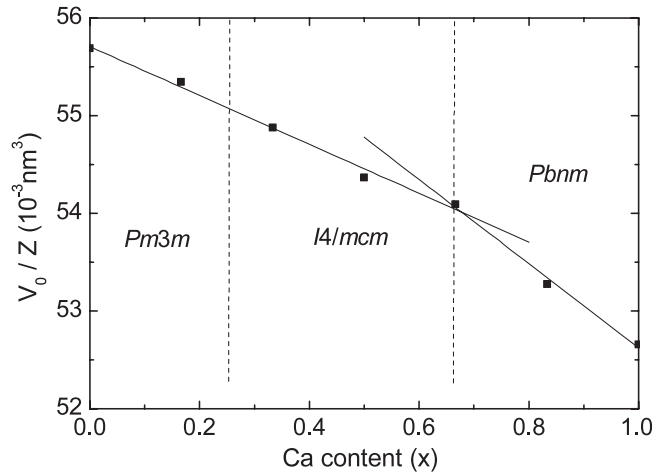


**Figure 3.** Calcium content ( $x$ ) dependence of the volume per formula ( $V_0/Z$ ) in the  $Sr_{1-x}Ca_xCrO_3$  family.

Table 1 summarizes the refined crystallographic data for the family of  $Sr_{1-x}Ca_xCrO_3$ . The crystal structural evolution observed in this study is consistent with previous reported results [6, 10, 11]. The  $x$  dependence of the unit-cell volume per molecular  $ACrO_3$  unit ( $V_0/Z$ ) obeys Végard’s law in the region  $0 \leq x \leq 2/3$  although a cubic-to-tetragonal phase transition occurs in this region; but as can be seen in figure 3, there is a discontinuity in the law, if not also in  $V_0/Z$  itself, where there appears to be a first-order change from tetragonal to orthorhombic symmetry at  $x = 2/3$ . Note that the present  $x - V_0/Z$  relationship is different from the reported results in [6]. This is probably related to the considerable amount of impurity in previous samples, which were prepared at 6.5 GPa and  $950^\circ C$  for all the intermediate  $x$  values. In this study, to obtain higher quality samples, the synthesis pressure was set to 6.0 GPa but the temperature was gradually changed from  $900$  to  $1200^\circ C$  with a step of  $25^\circ C$ . The data presented here were taken from the best sample for each composition.

### 3.2. Electric transport and magnetism at ambient pressure

Figures 4(a)–(c) show the temperature dependence of the resistivity  $\rho(T)$  for the  $x = 0, 1/2,$  and  $1.0$  samples, which are representative of the three different structural phases. Above 80 K, the  $\rho(T)$  of  $SrCrO_3$  is only weakly temperature dependent, and the data can be fitted by using a thermal activation model with the function  $\rho(T) \sim \exp(E_a/\kappa_B T)$ , as shown in the inset of figure 4(a). Here,  $E_a$  and  $\kappa_B$  present the Boltzmann constant and activation energy, respectively. The fitted  $E_a$  for the cubic  $SrCrO_3$  is  $5.6 \times 10^{-3}$  eV. A similar  $\rho(T)$  behavior above 150 K is found for the tetragonal sample with  $x = 1/2$ , but with an increased  $E_a = 1.8 \times 10^{-2}$  eV (see the inset of figure 4(b)). However, the  $\rho(T)$  of orthorhombic  $CaCrO_3$  is higher by about four orders of magnitude and fits to  $\rho(T) \sim \exp(T_0/T)^{1/4}$  as presented in the inset of figure 4(c), which is characteristic of Mott 3D variable-range hopping [15]. When a magnetic field (6 T) is applied for the cubic  $SrCrO_3$ , the  $\rho(T)$  curve is almost unchanged with respect to that for zero field. In the

**Table 1.** Crystal-structure parameters from the Rietveld refinements of  $\text{Sr}_{1-x}\text{Ca}_x\text{CrO}_3$ . (Note: in  $Pm\bar{3}m$  symmetry, Sr/Ca, Cr, and O occupy the special sites 1a (0, 0, 0), 1b (0.5, 0.5, 0.5), and 3c (0.5, 0.5, 0), respectively. In the  $I4/mcm$  space group, Sr/Ca, Cr, O1, and O2 occupy the special sites 4b (0, 0.5, 0.25), 4c (0, 0, 0), 4a (0, 0, 0.25), and 8h ( $x, y, 0$ ), respectively. In  $Pbnm$  symmetry, Ca/Sr and O1 occupy the special sites 4c ( $x, y, 0.25$ ), and Cr occupies the special site 4b (0.5, 0, 0).)

$x$	0	1/6	1/3	1/2	2/3	2/3	5/6	1
Space group	$Pm\bar{3}m$	$Pm\bar{3}m$	$I4/mcm$	$I4/mcm$	$I4/mcm$	$Pbnm$	$Pbnm$	$Pbnm$
$Z$	1	1	4	4	4	4	4	4
$a$ (Å)	3.818 71(6)	3.810 92(5)	5.372 70(9)	5.3539(1)	5.3446(3)	5.3403(8)	5.3189(4)	5.2914(3)
$b$ (Å)						5.3490(7)	5.3289(5)	5.3140(4)
$c$ (Å)			7.6045(2)	7.5866(3)	7.5735(9)	7.5744(7)	7.5185(6)	7.4902(4)
$V_0$ (Å <sup>3</sup> )	55.687(2)	55.346(1)	219.511(8)	217.46(2)	216.33(3)	216.36(3)	213.10(2)	210.62(2)
$x(\text{Sr/Ca})$	0	0	0	0	0	0.998(2)	0.997(1)	0.999(1)
$y(\text{Sr/Ca})$	0	0	0.5	0.5	0.5	0.0081(5)	0.0092(6)	0.0277(3)
$x(\text{O1})$	0.5	0.5	0	0	0	0.029(3)	0.027(2)	0.099(2)
$y(\text{O1})$	0.5	0.5	0	0	0	0.217(3)	0.287(2)	0.478(1)
$x(\text{O2})$			0.2395(9)	0.227(1)	0.222(1)	0.781(3)	0.707(2)	0.719(1)
$y(\text{O2})$			0.2605(9)	0.273(1)	0.279(1)	0.217(3)	0.287(2)	0.279(1)
$z(\text{O2})$			0	0	0	0.025(1)	0.046(1)	0.030(6)
$\langle\text{Cr-O}\rangle$ (Å)	1.909 35(6)	1.905 46(5)	1.901 19(4)	1.899 03(6)	1.8990(1)	1.907(2)	1.923(7)	1.917(7)
Cr–O1–Cr (deg)	180	180	180	180	180	170.6(8)	65.2(5)	148.0(5)
Cr–O2–Cr (deg)	180	180	175.2(4)	169.4(5)	167.0(6)	161.5(4)	152.6(4)	160.7(2)
$\langle\text{Cr-O-Cr}\rangle$ (deg)	180	180	176.8(3)	172.9(3)	171.0(4)	164.5(5)	156.8(4)	156.5(3)
$\langle\varphi\rangle$ (deg) <sup>a</sup>	0	0	1.6(2)	3.6(2)	4.5(2)	7.8(3)	11.6(2)	11.8(2)
$R_p$ (%)	6.18	5.88	6.90	8.15	8.69	8.23	7.23	7.82
$R_{wp}$ (%)	9.77	9.59	9.71	10.85	10.92	10.56	9.64	9.71

$$^a \langle\varphi\rangle = (180 - \langle\text{Cr-O-Cr}\rangle)/2.$$

**Table 2.** Antiferromagnetic transition temperatures  $T_N$  (K) of the  $\text{Sr}_{1-x}\text{Ca}_x\text{CrO}_3$  family. (Note: C = cubic, T = tetragonal, O = orthorhombic.)

$x$	0	1/6	1/3	1/2	2/3	5/6	1
Phase	C	C	T	T	T + O	O	O
$T_N$	—	—	41	52	57	83	90

orthorhombic  $\text{CaCrO}_3$ , however, a field of 6 T induces a small, positive magnetoresistance below 150 K. A smaller positive magnetoresistance at 6 T can also be seen below 50 K in the tetragonal phase with  $x = 1/2$ . The low temperature anomalies in resistivity around 90 K in  $\text{CaCrO}_3$  and near 50 K in  $\text{Sr}_{0.5}\text{Ca}_{0.5}\text{CrO}_3$  reflect the onsets of long-range antiferromagnetic transitions.

The magnetic behavior observed in this study is similar to that in previous reports [2, 6]. There is no long-range magnetic order in the cubic phase; long-range antiferromagnetic order is found in the tetragonal phase; weak ferromagnetic behavior due to the canted antiferromagnetism is shown in the orthorhombic phase. The magnetic transition temperatures are listed in table 2, but we do not show the detailed magnetization curves in this paper.

### 3.3. The pressure-induced insulator–metal transition

Figure 5 shows the pressure-dependent resistance at 280 K for three representative phases: the cubic  $\text{SrCrO}_3$ , the tetragonal  $\text{Sr}_{2/3}\text{Ca}_{1/3}\text{CrO}_3$ , and the orthorhombic  $\text{CaCrO}_3$ . A sharp initial decrease in resistance with applied pressure is evident in these samples. The temperature dependence of

the resistance of these three samples, plotted as  $\ln R(T)$ , is shown for several pressures in figures 6(a)–(c). The insets show that the slopes  $dR(T)/dT$  change sign at a critical temperature  $T_{IM}(P)$  that decreases with increasing pressure. In  $\text{SrCrO}_3$ ,  $T_{IM}$  falls below 300 K for pressures  $P > 5.4$  GPa; in  $\text{Sr}_{2/3}\text{Ca}_{1/3}\text{CrO}_3$  and  $\text{CaCrO}_3$  this occurs at pressures  $P > 15.0$  GPa.

## 4. Discussion

An itinerant-electron model of the  $\text{CrO}_3$  array of the  $\text{Sr}_{1-x}\text{Ca}_x\text{CrO}_3$  system would have an antibonding band of t-orbital parentage, 1/3 filled. However, on the approach to a transition from itinerant to localized electronic behavior, the on-site electrostatic energy  $U_\pi$  may create an energy gap between the  $\text{Cr}^{5+}/\text{Cr}^{4+}$  and  $\text{Cr}^{4+}/\text{Cr}^{3+}$  redox couples that is larger than the  $\pi^*$  bandwidth, i.e.  $W_\pi < U_\pi$ . Our previous measurements [2] of the thermoelectric power for  $\text{SrCrO}_3$  and  $\text{CaCrO}_3$  have indicated a small overlap of the  $\text{Cr}^{5+}/\text{Cr}^{4+}$  and  $\text{Cr}^{4+}/\text{Cr}^{3+}$  redox couples ( $W_\pi \approx U_\pi$ ) in  $\text{SrCrO}_3$  and a  $U_\pi > W_\pi$  in  $\text{CaCrO}_3$ .

Actually, the existence of the  $\text{Cr}_2\text{O}_3$  impurity signals that Cr vacancies are present; the presence of Cr vacancies means not only that the  $\text{CrO}_3$  array is somewhat oxidized, which lowers the Fermi energy  $E_F$  into the  $\text{Cr}^{5+}/\text{Cr}^{4+}$  couple, but also that there is a perturbation of the periodic potential that would introduce Anderson-localized states [16] above a mobility edge  $\mu_C$  at the top of the  $\text{Cr}^{5+}/\text{Cr}^{4+}\pi^*$  redox band. An  $E_F > \mu_C$  would have localized states at  $E_F$ , and an  $E_F < \mu_C$  would have itinerant-electron states at  $E_F$ . As  $E_F$  approaches  $\mu_C$  from above, thermal excitation of electrons from the itinerant-electron density of states to

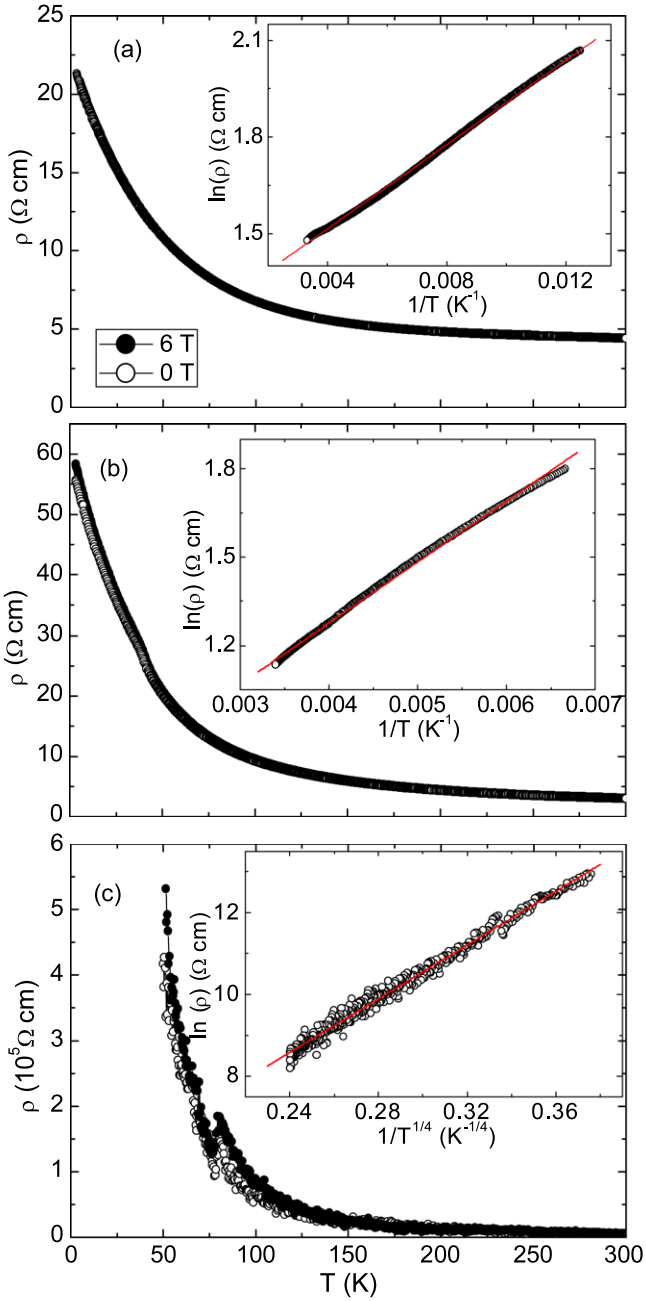


**Figure 4.** Temperature dependence of the resistivity at ambient pressure and 0 T (open circles) and 6 T (solid circles) for (a)  $x = 0$ , (b)  $x = 1/2$ , and (c)  $x = 1$  in the  $\text{Sr}_{1-x}\text{Ca}_x\text{CrO}_3$  family. The solid lines in the insets show the fitting results as described in the text.

the localized states above  $E_F$  introduces itinerant-electron holes below  $\mu_C$ . However, a large  $E_F - \mu_C$  energy would mean that variable-range hopping between the localized states above  $\mu_C$  would, at lower temperatures, compete with thermal excitation of electrons from below  $\mu_C$ . Moreover, the presence of localized-electron fluctuations would decrease the thermal conductivity as previously observed in  $\text{SrCrO}_3$  and  $\text{CaCrO}_3$  [2]. According to this model, increasing the width of the  $\pi^*$  band lowers  $E_F$  relative to  $\mu_C$  for a fixed occupancy of the  $\pi^*$  band; and at a critical bandwidth,  $E_F$  crosses  $\mu_C$  to create itinerant electrons at  $E_F$  and,

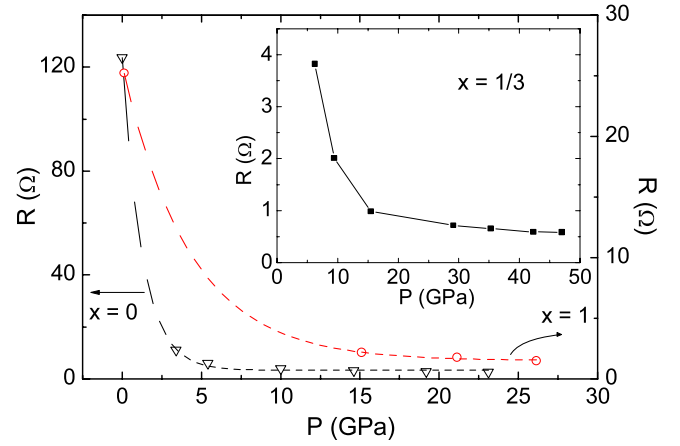


**Figure 5.** Pressure dependence of the resistance for  $x = 0, 1/3$  (inset), and  $x = 1$  samples in the  $\text{Sr}_{1-x}\text{Ca}_x\text{CrO}_3$  family at 280 K.

therefore, metallic conductivity. In order to interpret the observation of the insulator–metal transition at  $T_{\text{IM}}(P)$  and the other observations, we must consider how the structure and bandwidth are influenced by substitution of  $\text{Sr}^{2+}$  by  $\text{Ca}^{2+}$  ions.

The tight-binding bandwidth is  $W_\pi \approx 12b_\pi$ , where  $b_\pi \approx \varepsilon_\pi(\psi_i, \psi_j)$  is the expectation for an electron hop between nearest-neighbor Cr atoms. The overlap integral  $(\psi_i, \psi_j)$  of the ligand-field t orbitals on neighboring Cr atoms at  $\mathbf{R}_i$  and  $\mathbf{R}_j$  increases with the covalent admixture into the t orbitals of the 2p orbitals of the bridging oxygen that  $\pi$ -bond with the Cr t orbitals. Because the  $\text{Cr}^{4+}/\text{Cr}^{3+}$  empty redox couple lies close to the top of the O 2p bands, the covalent admixture of O 2p into the ligand-field t orbitals is large enough to give a significant  $(\psi_i, \psi_j)$  overlap integral over the bridging oxygen. Moreover, there is no contribution from the cubic-field splitting of the Cr 3d electronic states to the intra-atomic electrostatic energy  $U_\pi$  that inhibits formation of itinerant-electron states. Consequently, we find a  $W_\pi \approx U_\pi$  in the  $\text{CrO}_3$  array as is made evident by the antiferromagnetic order in  $\text{CaCrO}_3$  and the lack of long-range magnetic order in  $\text{SrCrO}_3$ .

We note that the substitution of  $\text{Ca}^{2+}$  for  $\text{Sr}^{2+}$  in the present  $\text{Sr}_{1-x}\text{Ca}_x\text{CrO}_3$  family has two effects: one is physical, which influences primarily the structure, and the other is chemical, which has the more important influence on  $W_\pi$ . The smaller size of the  $\text{Ca}^{2+}$  ion decreases the geometric tolerance factor  $t_1 \equiv (\text{A-O})/[\sqrt{2}(\text{Cr-O})]$ , where  $(\text{A-O})$  is the mean equilibrium Sr/Ca–O bond length of A-site cations and  $(\text{Cr-O})$  is the equilibrium Cr–O bond length. In general, an ideal cubic-perovskite structure is found for a  $t_1 \approx 1$ ; the structure adjusts to  $t_1 < 1$  by introducing cooperative octahedral rotations. The orthorhombic  $Pbnm$  rotations are commonly found for  $t_1 < 1$ ; but the transition from orthorhombic to cubic symmetry as  $t_1 < 1$  increases to  $t_1 \approx 1$  is not second order. Rotations that give tetragonal or rhombohedral symmetry may be found in the tolerance-factor interval between that for the orthorhombic structure and the  $t_1 \approx 1$  for the cubic structure. The observation of a

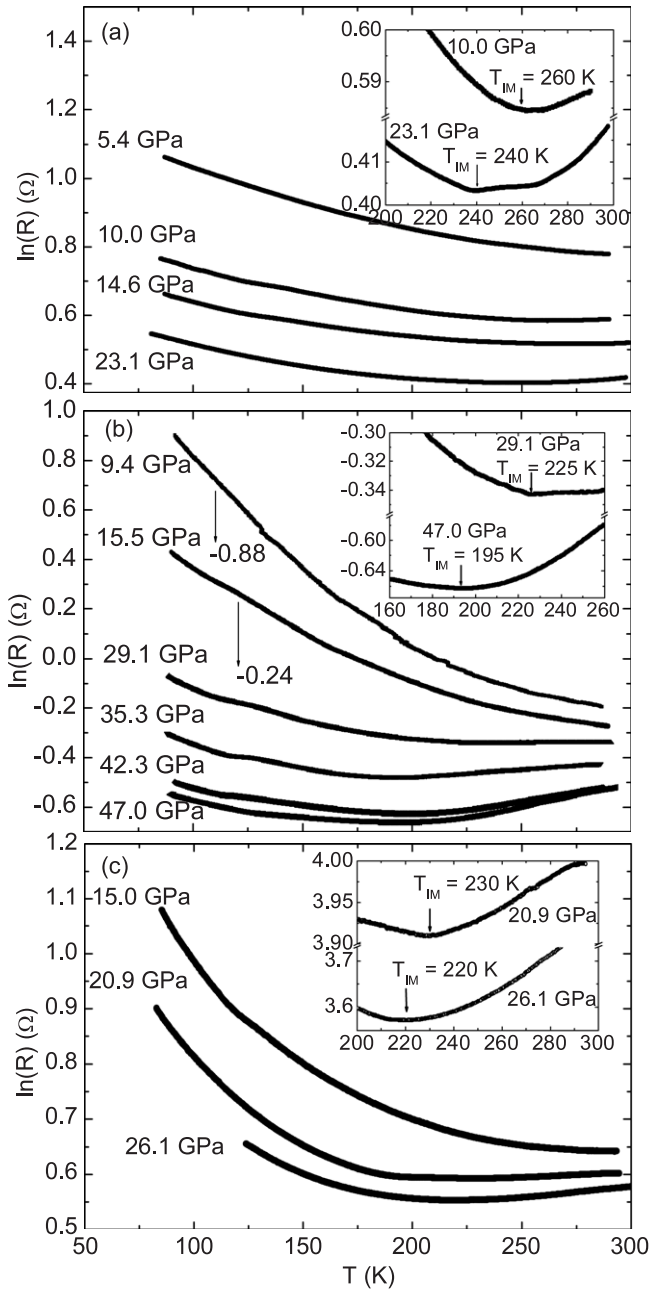


**Figure 6.** Temperature dependence of the resistance of (a) SrCrO<sub>3</sub>, (b) Sr<sub>2/3</sub>Ca<sub>1/3</sub>CrO<sub>3</sub>, and (c) CaCrO<sub>3</sub> at various pressures. The insets zoom into the pressure-induced insulator–metal transitions at several representative pressures. For clarity, the resistance data at 9.4 and 15.5 GPa in (b) were shifted antiparallel to the y axis by 0.88 and 0.24 unit, respectively.

tetragonal phase in the Sr<sub>1-x</sub>Ca<sub>x</sub>CrO<sub>3</sub> system between the cubic SrCrO<sub>3</sub> and orthorhombic CaCrO<sub>3</sub> is primarily due to the physical effect of substituting a smaller Ca<sup>2+</sup> ion for Sr<sup>2+</sup>, which lowers the tolerance factor. Although the cooperative octahedral-site rotations bend the Cr–O–Cr bond angle from 180°, any lowering of the ( $\psi_i, \psi_j$ ) overlap integral for the  $\pi$ -bonding electrons due to this bending is small.

The more important influence on  $W_\pi$  is chemical in origin. Chemically, the Ca<sup>2+</sup> ion is more acidic than the

Sr<sup>2+</sup> ion, which makes it compete more strongly for the O 2p orbitals. Since the O 2p orbitals that  $\pi$ -bond with the Cr t orbitals also  $\sigma$ -bond with the alkaline-earth atoms, this competition reduces the covalent O 2p admixture into the Cr t ligand-field orbitals and therefore the overlap integral of  $b_\pi$ . Any influence of the A-site cation on the one-electron energy  $\epsilon_\pi$  of  $b_\pi$  is not obvious, but it is universally observed that the substitution of smaller, more acidic A-site cations in the AMO<sub>3</sub> perovskites narrows  $\pi^*$  bands and that the chemical influence is more important than the bending of the M–O–M bond [17–20].

From this analysis, we conclude that stoichiometric SrCrO<sub>3</sub> contains itinerant  $\pi^*$  electrons in a Cr<sup>5+</sup>/Cr<sup>4+</sup> redox couple having a bandwidth  $W_\pi \approx U_\pi$ . The instability of a  $W_\pi \approx U_\pi$  may be the origin of the stabilization of some oxidation of the CrO<sub>3</sub> array by the introduction of cation vacancies [21]; these vacancies perturb the periodic potential sufficiently to introduce Anderson-localized states above a mobility edge  $\mu_C$  at the top of the Cr<sup>5+</sup>/Cr<sup>4+</sup> couple. For a fixed oxidation state of the CrO<sub>3</sub> array, the position of the Fermi energy  $E_F$  with respect to  $\mu_C$  is lowered by a broadening of  $W_\pi$ . The transport data for SrCrO<sub>3</sub>, figure 4(a), suggest an  $E_F$  only a few meV above  $\mu_C$ , which results in semiconducting behavior with a small activation energy below 300 K. The primary experimental results of synchrotron XRD under high pressure reveal no change in crystal structure for SrCrO<sub>3</sub> and CaCrO<sub>3</sub> [22], indicating that the pressure-induced metallization is due to broadening of  $W_\pi$  by increasing its O 2p character. The application of hydrostatic pressure broadens  $W_\pi$  to reduce  $E_F - \mu_C$  until, above 5.4 GPa for example in SrCrO<sub>3</sub>,  $E_F$  falls below  $\mu_C$  and the sample becomes metallic above  $T_{IM} < 300$  K as shown in figure 6(a);  $T_{IM}$  falls to lower temperatures as  $W_\pi$  increases with pressure. Similar behaviors occur in the tetragonal and orthorhombic phases in the Sr<sub>1-x</sub>Ca<sub>x</sub>CrO<sub>3</sub> family with increasing pressure (figures 6(b) and (c)). Moreover, electrons in Anderson-localized states may introduce localized spins that introduce a temperature-dependent component to the paramagnetic susceptibility; but these spins are not expected to give long-range magnetic order at low temperatures. The paramagnetic susceptibility of SrCrO<sub>3</sub> reveals no evidence of long-range magnetic order above 5 K, but a small difference between the zero field cooled and field cooled curves below 50 K may reflect the onset of some short-range magnetic order [2]. The same type of spin order may also take place below 50 K in the  $x = 1/6$  sample. The initial sharp drop in resistance with applied pressure in our polycrystalline samples (figure 5) shows the presence of a significant grain-boundary resistance that could be responsible for the small activation energies of the resistivity in the  $x = 0$  and  $1/6$  samples. Recently, a poor metallic behavior was predicted in theory and also detected from optical measurements for CaCrO<sub>3</sub> [23, 24]. However, electric measurement on the same sample suggested a nonmetallic state with  $\rho > 1000 \Omega \text{ cm}$  at low temperature. It looks as if the grain boundaries play a role in the electric transport properties in the Sr<sub>1-x</sub>Ca<sub>x</sub>CrO<sub>3</sub> family. The grain-boundary effects may also be  $x$  dependent in this system, but they should not influence qualitatively the results that we concluded in this study.

The structural data of figure 3 signal that an important change in the electronic properties may occur at a first-order transition from tetragonal to orthorhombic symmetry near  $x = 2/3$ . It has been argued from the virial theorem [25] that more localized, i.e. more strongly correlated, electrons have a longer equilibrium (M–O) bond length, but figure 3 shows that  $V_0/Z$  versus  $x$  for  $0 \leq x < 2/3$  falls below the extrapolation of Végard's law for the orthorhombic phase in the range  $2/3 < x \leq 1.0$ . However, a reduction in the Cr–O–Cr bond angle in the orthorhombic phase can not only accommodate a larger Cr–O bond length, but also introduces a shorter competitive Ca–O bond. Therefore, we conclude that in the orthorhombic phase, the Cr 3d electrons are more strongly correlated, i.e. are more tightly bound, even though the superexchange interaction cannot be described by the localized-electron second-order perturbation theory. Moreover, the transport data of figure 4(c) are consistent with a large  $E_F - \mu_C$ . However, variable-range hopping rather than small-polaron behavior of the holes in the  $\text{Cr}^{5+}/\text{Cr}^{4+}$  couple suggests that the  $\pi^*$  electrons give rise to a band antiferromagnetism rather than a localized-electron antiferromagnetism. This conclusion is reinforced by the observation [10] of  $dT_N/dP < 0$  in  $\text{CaCrO}_3$  and also by the increase in  $T_N$  from 83 to 90 K as  $x$  increases from 5/6 to 1.0 shown in table 2. Where the superexchange perturbation theory is valid [26], an increase in  $b_\pi$  would increase  $T_N \sim b_\pi^2/\Delta E$ , and a reduction in  $b_\pi$  would decrease  $T_N$ .

For the interval  $0 < x < 1.0$ , we comment qualitatively on the evolution with  $x$  of the physical properties without consideration of the effect of the variance introduced by the coexistence of two different A-site cations. The smaller  $\text{Ca}^{2+}$  ion lowers the tolerance factor  $t_1$ , inducing increasing cooperative rotations of the  $\text{CrO}_{6/2}$  octahedral sites as  $x$  increases. The cubic-to-tetragonal transition may be smooth; it does not introduce any local octahedral-site distortion that would bias orbital order. However, narrowing of  $W_\pi$  and bending of the Cr–O–Cr bond angles in the  $a$ - $b$  plane induce long-range antiferromagnetic order of the  $\pi^*$  electrons with a  $T_N$  that increases with decreasing  $W_\pi$ . We can predict that the magnitude of the spin density of a Cr site may also increase with  $x$ . In the tetragonal phase, the spins are not canted, and we predict that they are oriented along the  $c$  axis in the tetragonal structure. However, the tetragonal–orthorhombic transition is first order, and the larger bending of the Cr–O–Cr angle, to  $156^\circ$  in  $\text{CaCrO}_3$ , is accompanied by local site distortions that bias ordering of the  $t$  orbitals as in  $\text{YVO}_3$ , which has a localized  $V^{3+};t^2e^0$  configuration. A recent neutron-diffraction study [24] shows the same orbital and magnetic order setting in below  $T_N$  in  $\text{CaCrO}_3$  as is found in  $\text{LaVO}_3$ .

## 5. Conclusion

We have synthesized at 6.0 GPa and 900–1200 °C the polycrystalline  $\text{Sr}_{1-x}\text{Ca}_x\text{CrO}_3$  perovskite solid solution in steps of  $x = 1/6$  over the range  $0 \leq x \leq 1$ . Three room-temperature structures were observed: cubic for  $x = 0$  and  $1/6$ , tetragonal for  $x = 1/3$  and  $1/2$ , and orthorhombic for  $x = 5/6$  and 1, in agreement with previous reports

[6, 10, 11]. The tetragonal and orthorhombic phases coexisted in the  $x = 2/3$  sample, characteristic of a first-order change between these phases. No long-range magnetic order occurs in the cubic phase, whereas long-range antiferromagnetic order appears in the tetragonal and orthorhombic phases with  $T_N$  increasing with  $x$ . In both  $\text{CaCrO}_3$  and  $\text{LaVO}_3$ , orbital ordering below  $T_N$  resolves the orbital–spin frustration of the superexchange interaction responsible for the magnetic order. It would be of interest to know whether a similar resolution occurs below  $T_N$  in the more itinerant antiferromagnetism of the tetragonal phase.

The evolution of the structure is well understood from the decrease in the geometric tolerance factor; it follows the pattern observed for all  $\text{AMO}_3$  perovskite families. Moreover, the evolution of electronic properties can be understood to be due to a narrowing of the  $\pi^*$  band of itinerant electrons with  $\text{Ca}^{2+}$  substitution for  $\text{Sr}^{2+}$ ; this narrowing is characteristic of other perovskites as a result of a greater competition of the smaller, more acidic A cation for the O 2p orbitals that  $\pi$ -bond with the  $\pi$ -bonding d orbitals on the transition metal M cations. A slight oxidation of the  $\text{CrO}_3$  array is characteristic of lattice instabilities found in perovskites near the transition from itinerant to localized electronic behavior. The introduction of cation vacancies and the variances associated with the coexistence of two different A-site cations complicates a quantitative analysis of the evolution of physical properties with  $x$ , but the model of a  $\pi^*$  band with a width  $W_\pi \approx U_\pi$  allows a straightforward rationalization of the observed data, indicating a crossover from itinerant-electron to localized-electron behavior in  $\text{Sr}_{1-x}\text{Ca}_x\text{CrO}_3$  solid solution [2, 4, 24].

## Acknowledgments

This work was supported by NSF and MOST of China through research projects, the NSF of the US, and the Robert A Welch Foundation of Houston, TX, Grant no. F-1066.

## References

- [1] Goodenough J B 1967 *Czech. J. Phys.* **17** 304
- [2] Zhou J-S, Jin C Q, Long Y W, Yang L X and Goodenough J B 2006 *Phys. Rev. Lett.* **96** 046408
- [3] Ortega-San-Martin L, Williams A J, Rodgers J, Attfield J P, Heymann G and Huppertz H 2007 *Phys. Rev. Lett.* **99** 255701
- [4] Streltsov S V, Korotin M A, Anisimov V I and Khomskii D I 2008 *Phys. Rev. B* **78** 054425
- [5] Lee K W and Pickett W E 2009 *Phys. Rev. B* **80** 125133
- [6] Castillo-Martínez E, Durán A and Alario-Franco M Á 2008 *Solid State Chem.* **181** 895
- [7] Castillo-Martínez E, Arévalo-López A M, Ruiz-Bustos R and Alario-Franco M A 2008 *Inorg. Chem.* **47** 8526
- [8] Zhou J-S and Goodenough J B 2008 *Phys. Rev. B* **77** 132104
- [9] Zhou J-S, Ren Y, Yan J-Q, Mitchell J F and Goodenough J B 2008 *Phys. Rev. Lett.* **100** 046401
- [10] Goodenough J B, Longo J M and Kafalas J A 1968 *Mater. Res. Bull.* **3** 471
- [11] Weiher J F, Chamberland B L and Gillson J L 1971 *J. Solid State Chem.* **3** 529

- [12] Larson A C and Von Dreele R B 2004 General Structure Analysis System (GSAS) *Los Alamos National Laboratory Report* LAUR 86
- [13] Mao H K, Xu J and Bell P M 1986 *J. Geophys. Res.* **91** 4673
- [14] Glazer A M 1972 *Acta Crystallogr. B* **28** 3384  
Glazer A M 1975 *Acta Crystallogr. A* **31** 756
- [15] Mott N F 1974 *Metal-Insulator Transitions* (London: Taylor and Francis) p 35
- [16] Anderson P W 1958 *Phys. Rev.* **109** 1492
- [17] Chmaissem O *et al* 2001 *Phys. Rev. B* **64** 134412
- [18] Garcya-Jaca J *et al* 1999 *Mater. Res. Bull.* **34** 289
- [19] Jin C Q *et al* 2008 *Proc. Natl Acad. Sci. USA* **105** 7115
- [20] Goodenough J B and Zhou J-S 2001 *Struct. Bond.* **98** 17
- [21] For example, see Dougier P, Fan J C C and Goodenough J B 1975 *J. Solid State Chem.* **14** 247
- [22] Long Y W *et al* 2006 *Proc. SRMS-5: 5th International Conference on Synchrotron Radiation in Materials Science (Chicago, IL, 30 July–2 August 2006)* p 188
- [23] Bhohe P A *et al* 2011 *Phys. Rev. B* **83** 165132
- [24] Komarek A C *et al* 2008 *Phys. Rev. Lett.* **101** 167204
- [25] Goodenough J B 2001 *Struct. Bond.* **98** 1
- [26] Goodenough J B 1971 *Prog. Solid State Chem.* **5** 145